이학박사학위논문

Digital photolithography techniques for submicron pattern generation

마이크로미터 이하 패턴 제작을 위한 디지털 포토리소그래피 기술

2021년 8월

서울대학교 대학원

물리천문학부

강 민 수

Digital photolithography techniques for submicron pattern generation

마이크로미터 이하 패턴 제작을 위한 디지털 포토리소그래피 기술

지도교수 전 헌 수

이 논문을 이학박사 학위 논문으로 제출함

2021년 8월

서울대학교 대학원

물리천문학부

강 민 수

강민수의 박사학위 논문을 인준함

2021년 8월

위 원 장 _____ 차 국 린

부위원장 _____ 전 헌 수

위 원 _____ 이 탁 희

위 원 _____ 홍 성 철

위 원 _____ 최 성 환

Abstract

Digital photolithography techniques for submicron pattern generation

Minsu Kang

Department of Physics and Astronomy

The Graduate School

Seoul National University

Digital photolithography based on digital micromirror device (DMD) is considered the next-generation low-cost lithographic technology. However, DMD-based digital photolithography has been implemented only for micrometer-scale pattern generation, whereas sophisticated photonic devices require feature sizes of submicron.

In this thesis, we adopt a high-magnification imaging optical system for a custom-built digital photolithography system to generate submicron-scale patterns. We propose techniques to enhance the versatility of the digital photolithography, pattern tilting and grayscale exposure. We demonstrate that photonic crystal band-edge lasers of various lattice structures and periods can be quality-assessment testbeds.

We also tried to enhance pattern uniformity. The experimentally determined pixel spread function predicted the exposure result well, which means that we can improve the pattern quality through preliminary correction.

Keyword : Digital photolithography, Digital micromirror devices, Photonic crystal laser, Photonic crystal band-edge modes

Student Number : 2013-20349

Table of Contents

List of Figures

Chapter 1

Introduction

1.1. Photonic crystals

1.1.1. Introduction

A photonic crystal is an attractive structure to handle the photons [1]. Utilizing the photonic crystals, a laser device can be developed [2]. It can also be used as a testbed for topology photonics [3] or next-generation lithography [4].

Photonic crystals are composed of materials with different refractive indices to form a periodic structure. Based on the direction of the periodicity, it can be classified into 1, 2, and 3D photonic crystals (Figure 1-1). Electrons in the electronic crystal experience periodic atomic potential by periodic atoms. That is, the electronic band structure is determined as follows:

$$\left[-\frac{\hbar^2}{2m}\nabla^2 + V\right]\psi = E\psi$$

$$V(r) = V(r+R)$$

$$\psi(r) = \exp(ik\cdot r)\,u(r)$$

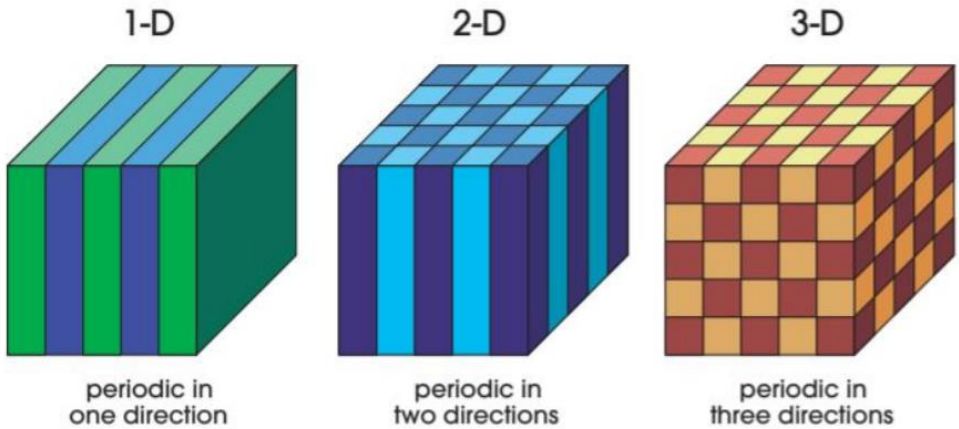

Figure 1-1. Examples of 1, 2, and 3D Photonic crystals [5].

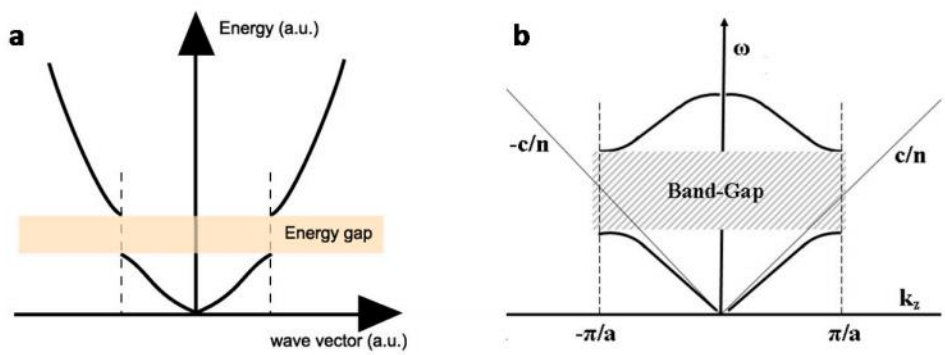

Figure 1-2. Analogy between the (a) energy gap in semiconductors and the (b) band-gap in photonic crystals [6].

Similarly, the photons in the photonic crystal experience periodic refractive indices by periodic materials. The photonic band structure which is known as photonic analogy can be derived using the equations below (Figure 1-2).

$$\nabla \times \left(\frac{1}{\varepsilon}\nabla \times H\right) = \left(\frac{\omega}{c}\right)^2 H$$

$$\varepsilon(r) = \varepsilon(r + R)$$

$$H(r) = \exp(ik \cdot r)\, u(r)$$

A band-edge mode and a defect cavity mode can be resonant modes of photonic crystals (Figure 1-3). Using these resonant modes, researchers can develop photonic crystal laser device.

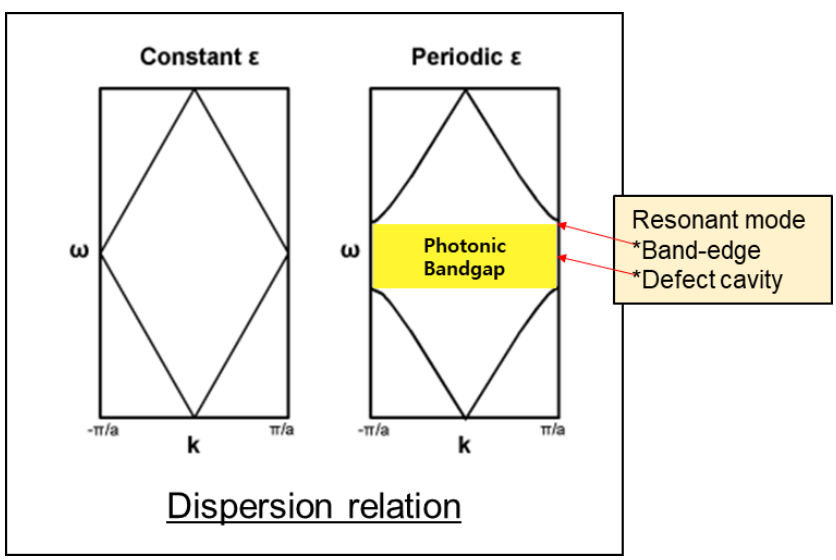

Figure 1-3. The resonant modes of photonic crystals.

1.1.2. Photonic crystal band-edge laser

The photonic crystal band-edge laser uses the effect of the decreasing group velocity and increasing effective gain near the band-edge of the photonic band structure.

$$\frac{g_{eff}}{g} = \frac{l_{eff}}{l} = \frac{c}{v_g}$$

Using the band-edge mode, it is possible to implement single mode laser operation. In addition, it is advantageous to develop a laser with high power and intended lasing direction utilizing the band-edge momentum (Figures 1-4 and 1-5).

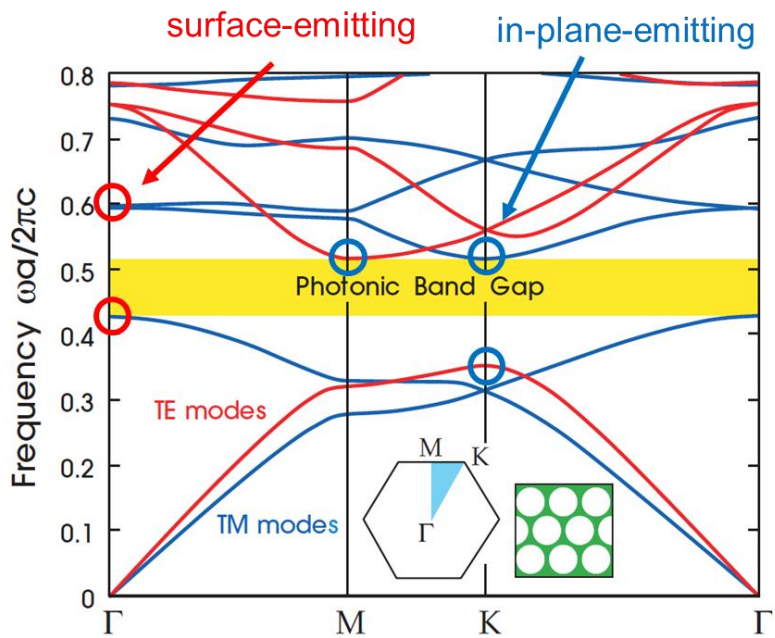

Figure 1-4. Band structure of hexagonal lattice and band-edge modes.

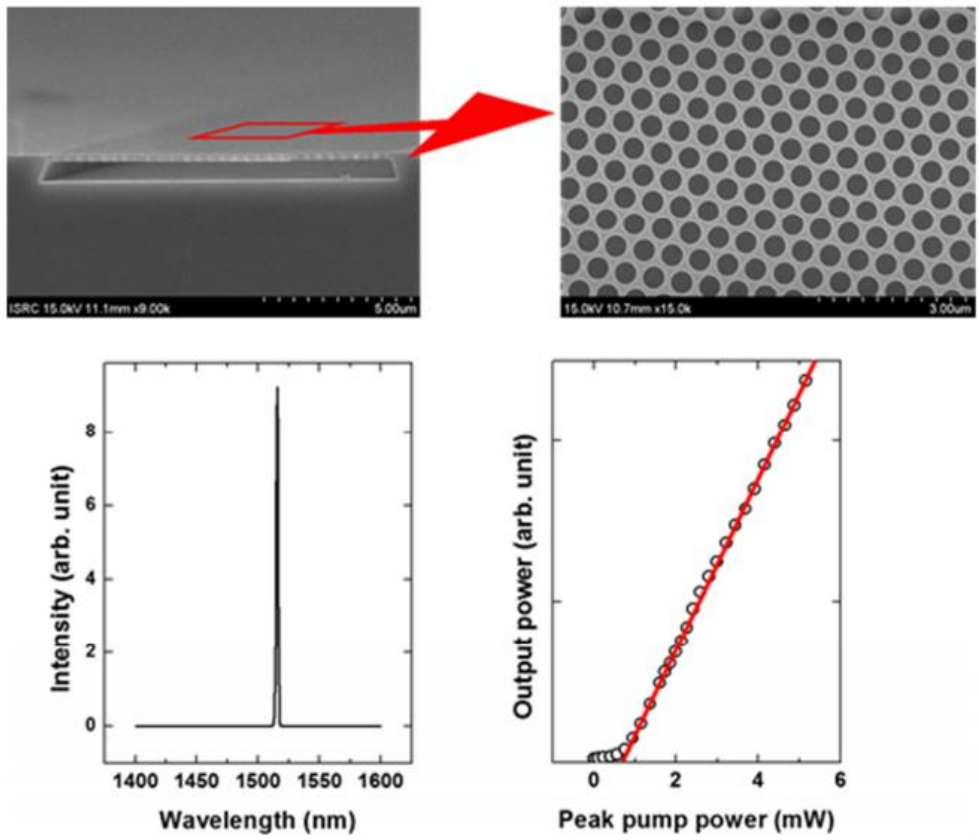

Figure 1-5. Hexagonal lattice photonic crystal band-edge laser [7].

1.1.3. Photonic crystal cavity laser

A defect structure is inserted into the photonic crystal cavity laser. When the light in the band−gap propagates inside the photonic crystal, it becomes an evanescent wave. That is, the photonic crystal region surrounding the defect structure acts as a mirror. As a result, a defect mode is generated inside the band-gap of the photonic band structure, and the photonic crystal cavity laser targets this defect mode. The photonic crystal cavity laser has the advantage of having a small mode volume and high Q factor, which is advantageous for low threshold lasing (Figures 1-6 and 1-7).

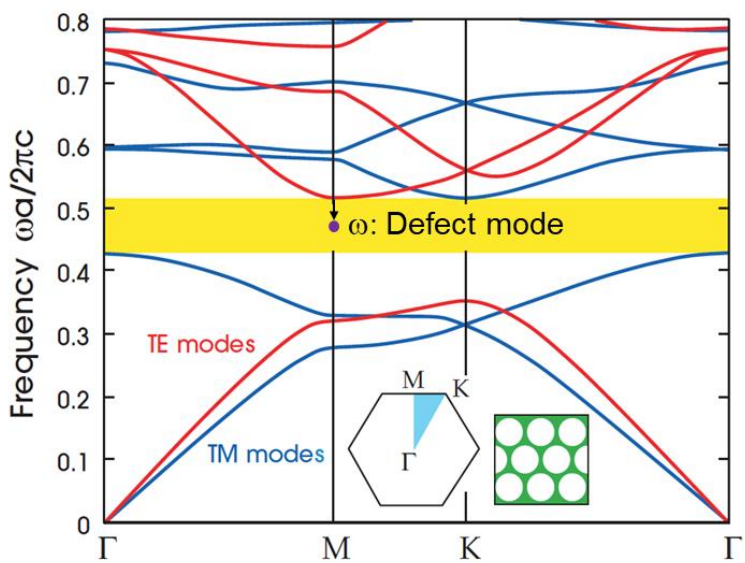

Figure 1-6. Band structure of hexagonal lattice and the defect mode.

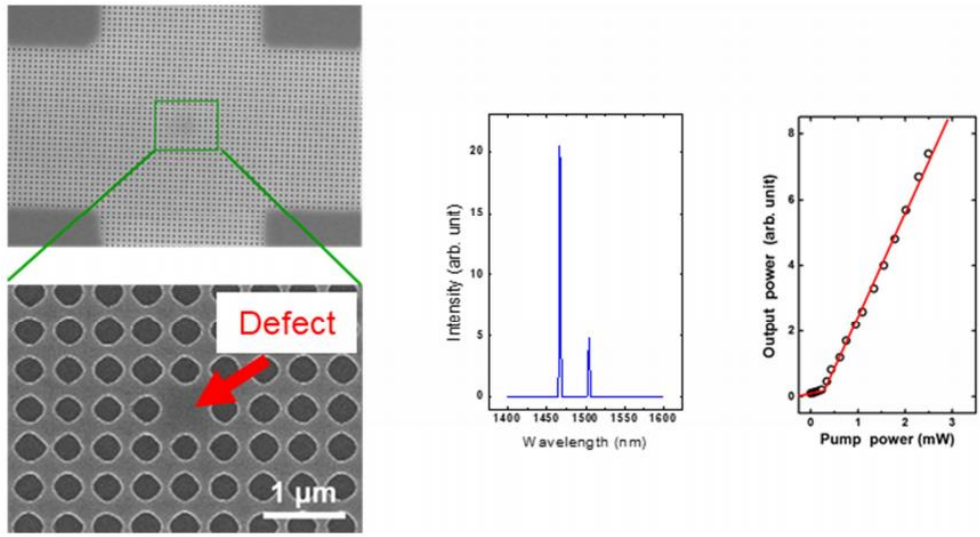

Figure 1-7. Hexagonal lattice photonic crystal cavity laser [8].

1.2. Conventional lithography techniques

The 2D patterning process is important for the fabrication of photonic crystal lasers. For the requirements for 2D patterning of photonic crystal laser fabrication, pattern production with submicron period and fine control of the pattern period is required. These requirements are fulfilled by electron beam (e-beam) lithography and laser interference lithography both of which are available at the laboratory. The resolution of e-beam lithography is high, however vacuum is required for exposure and the writing speed is slow (Figure 1-8). Exposure to a large area at once is possible with laser interference lithography, however only periodic structures with no defects can be fabricated (Figure 1-9).

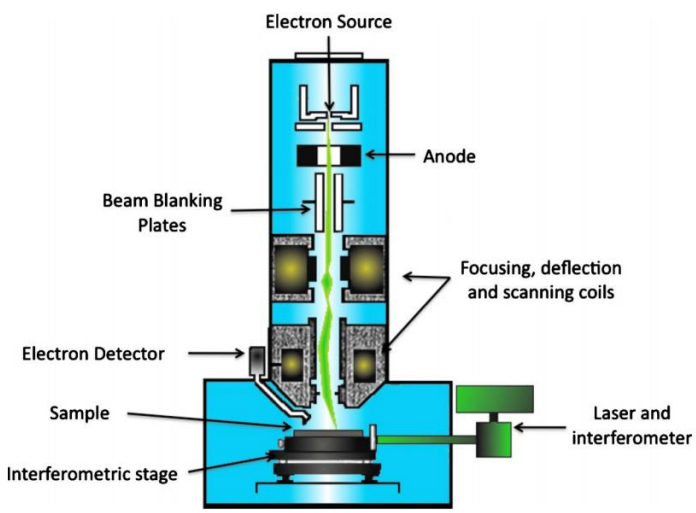

Figure 1-8. Structure of e-beam lithography system [9].

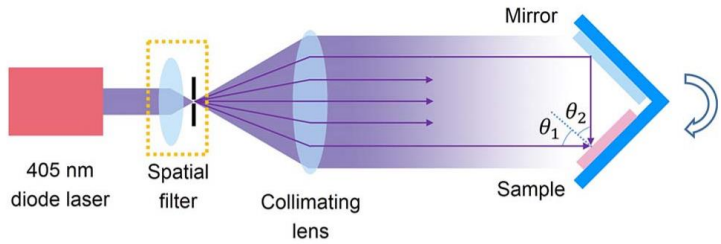

Figure 1-9. Structure of laser interference lithography system [10].

1.3. Alternative lithography technique: digital photolithography

To overcome the limitations of traditional lithography, digital photolithography with an electrically-addressed spatial light modulator as a dynamic mask has recently been used [11]. As shown in Figure 1-10, spatially processed light passing through the dynamic mask forms a pattern on the substrate through the imaging system. The digital micromirror device (DMD) is primarily used as electrically-addressed spatial light modulator. A DMD chip consists of millions of micromirrors which are connected to the lower MEMS structure. Light reflection can be spatially modulated by controlling each micromirror with the electrical signal.

Studies have been conducted to produce a variety of structures by digital photolithography. It is possible to produce not only 2D structures [12–15] but also 2.5D [16–23] and 3D structures [24–29]. In addition, image printing using magnetic ink or photobleaching of proteins has been reported. Because digital photolithography can reduce time, effort, and cost required to create a photomask, it is rapidly replacing traditional photolithography.

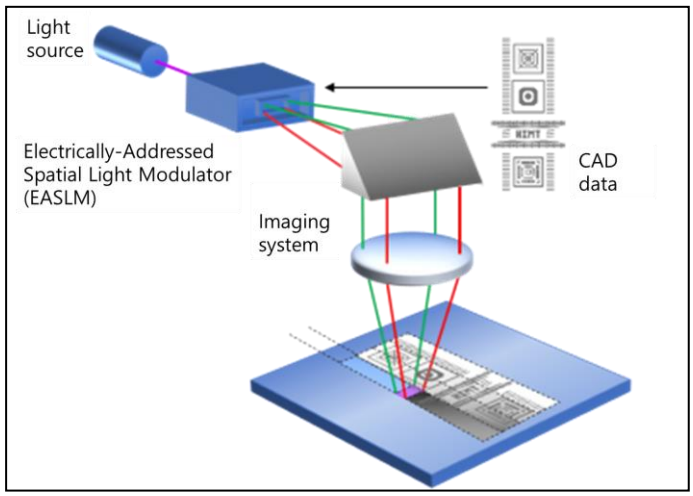

Figure 1-10. Electrically-addressed spatial light modulator based digital photolithography [30].

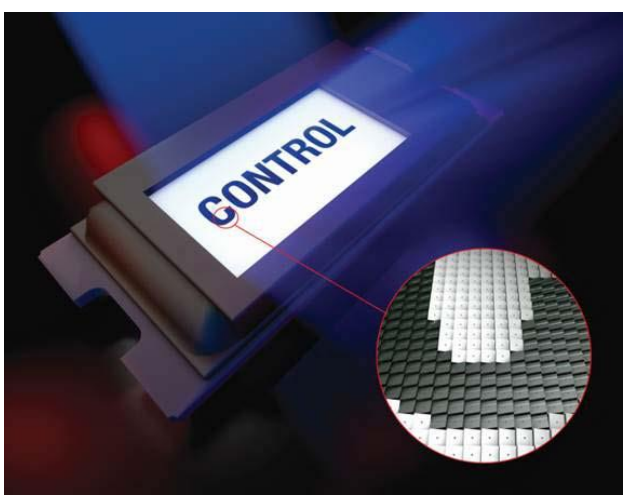

Figure 1-11. DMD as electrically-addressed spatial light modulator dynamic mask [31].

1.4. Outline of the manuscript

Figure 1-12 shows several digital lithography systems that have been reported so far in term of the pixel pitch at image plane and the smallest pattern period that can be produced using the system.

The minimum value of the smallest pattern period is 1.2 microns and the minimum value of pixel pitch at image plane is 100 nm. These values are relatively large in size, which are inadequate for developing photonic crystal laser device.

In this thesis, the aim is to develop the photonic crystal laser devices with the customized digital photolithography system.

In Chapter 2, a high-magnification imaging optical system for a custom-built digital photolithography system is used to generate submicron-scale patterns. The resolving power of the system was determined experimentally, and compared with the theoretical value.

In Chapters 3 and 4, pattern tilting and grayscale exposure are proposed and demonstrated to enhance the versatility of the digital photolithography system. The photonic crystal band-edge lasers of various lattice structures and periods were fabricated to demonstrated the performance of the system.

In Chapter 5, brightness correction was conducted through numerical analysis to improve the pattern quality. The photonic crystal cavity lasers were fabricated and it was reported that the correction affected the lasing properties.

Finally, in Chapter 6, the conclusion and perspective are presented.

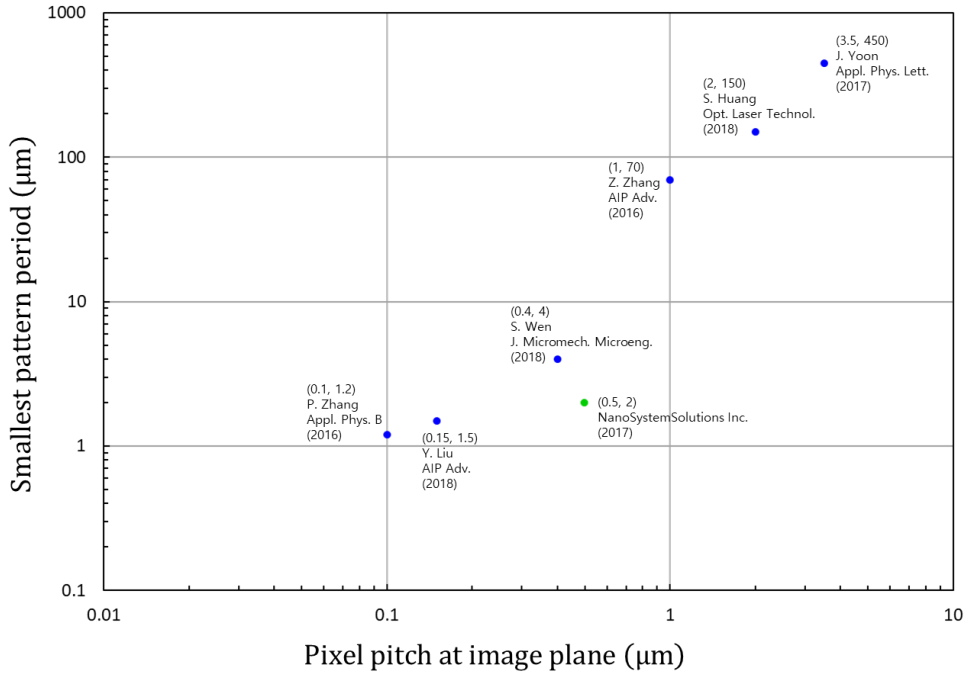

Figure 1-12. Various digital lithography systems.

Chapter 2

Submicron-scale digital photolithography

2.1. Introduction

2.1.1. Schematic of digital photolithography system

Figure 2-1 shows the basic structure of a digital photolithography system. The light incident on the DMD from the light source is reflected and an image of the DMD pattern is formed on the surface of the substrate through the projection optics.

The light reflected by the off-pixel does not pass through the projection optics, however only the light reflected by the on-pixel passes through the projection optics to form an image. Based on the configuration of the projection optics, the pixel pitch in the image plane may be larger or smaller than the micromirror pitch in the object plane.

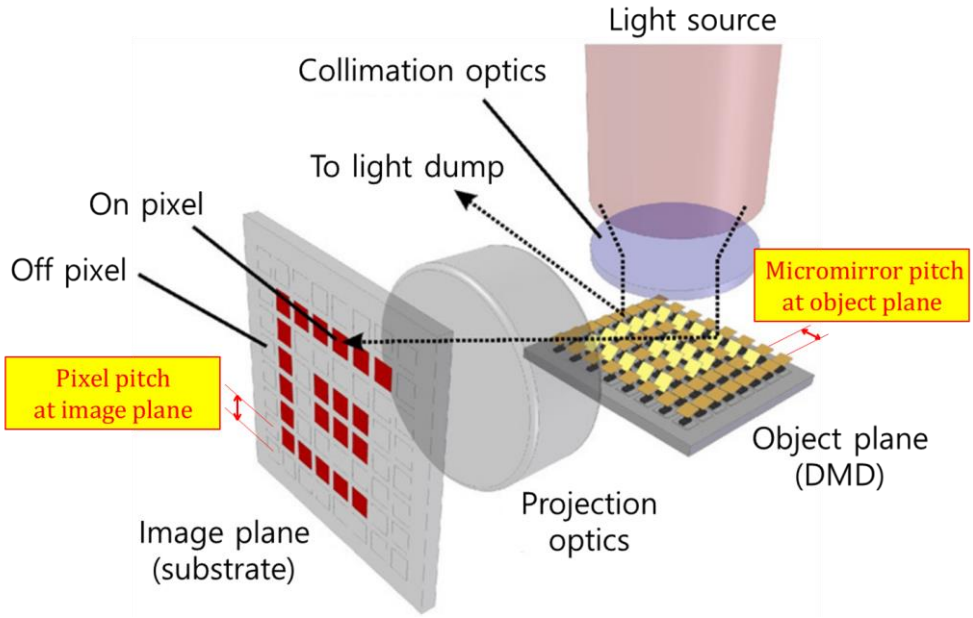

Figure 2-1. Basic structure of digital photolithography system [16].

2.1.2. Proposed digital photolithography system

A 4f-optical system which is commonly used in the image-forming optical system, was used to develop a digital photolithography system operating in dual mode, as shown in Figure 2-2.

The focusing mode is used to align the image plane with the sample surface. Using a 625 nm LED as a light source, it is possible to accurately focus while viewing through a CCD camera without the photochemical reaction of the photoresist (PR).

The exposure mode is used to record the DMD pattern on the photoresist. To trigger the photochemical reaction of the photoresist, a 405 nm LED is used as the light source of exposure mode.

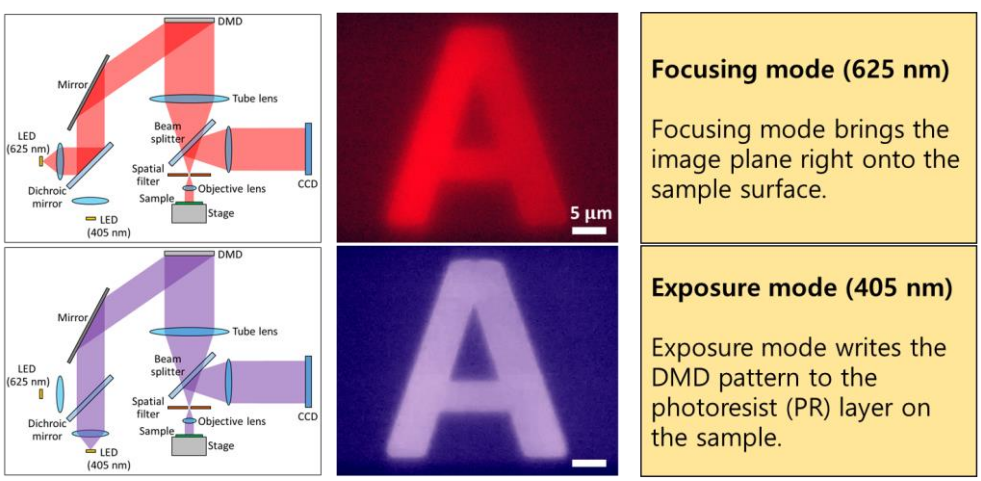

Figure 2-2. Two operation modes of proposed digital photolithography system.

2.1.3. Pixel pitch at image plane

The pixel pitch in the image plane is determined using the geometrical optics.

$$W = \frac{d}{\left(\frac{f_1}{f_2}\right)}$$

W = pixel pitch at image plane
d = micromirror pitch at object plane
f_1 = focal length of the tube lens
f_2 = focal length of the objective lens

The smaller the pixel pitch in the image plane, the finer the pattern period can be adjusted. To minimize the pixel pitch in the image plane, the DMD with the smallest micromirror pitch and the objective lens with the smallest focal length were combined (Figure 2-3). That is, combining DLP4710 DMD chip with CF Plan Apo 200 objective, the pixel pitch on the image plane was 29 nm. Moreover, because the objective with a large NA was used, the smallest pattern period that could be created was also smaller than those of other systems. The resolution of a photolithography system is determined by the Rayleigh's equation [32], and the Rayleigh criterion of proposed digital photolithography system was calculated to be approximately 274.5 nm.

$$R = k\frac{\lambda}{NA}$$

$$\begin{pmatrix} \text{where } R = \text{Rayleigh criterion}, k = \text{Rayleigh coefficient}, \\ \lambda = \text{wavelength}, NA = \text{numerical aperture of objective lens} \end{pmatrix}$$

Combination for the smallest pixel pitch

DMD

Part name	Micromirror pitch (μm)	Micromirror array size
DLP7000	13.6	1024x768
DLP5500	10.8	1024x768
DLP6500	7.6	1920x1080
DLP4710	5.4	1920x1080

Objective lens

Part name	Focal length (mm)	NA
CF Plan Apo 10	20	0.25
CF Plan Apo 50	4	0.55
CF Plan Apo 100	2	0.8
CF Plan Apo 200	1	0.9

Figure 2-3. The list of available DMD and objective lens.

2.1.4. Resolving power of proposed digital photolithography system

To grasp the resolving power of the system, the line gratings were exposed. The period of line gratings began from 19 pixels and gradually decreased by one pixel. Figure 2-4 shows the SEM image of the photoresist pattern on silicon substrate. The dark lines correspond to the areas illuminated by the exposure beam, where the photoresist is developed out. Each dark line was defined by a single DMD pixel line. Because the pattern period got closer to the Rayleigh criterion, the sharpness of the pattern gradually decreased. If the period was less than 12 pixels, it was difficult to identify the pattern with SEM.

SEM image	a	
	nm	p
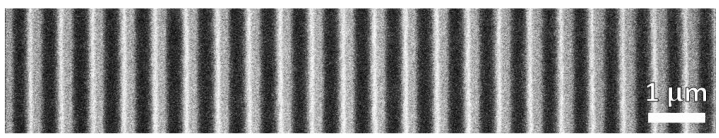	542.6	19
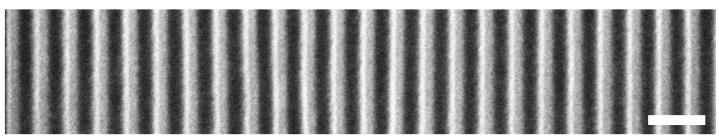	514.1	18
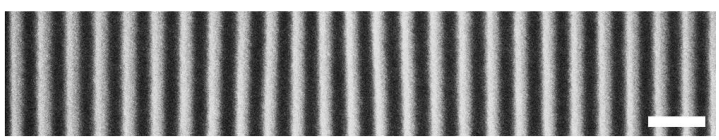	485.5	17
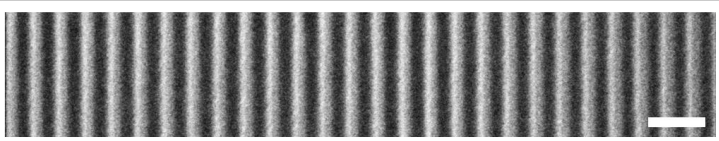	457.0	16
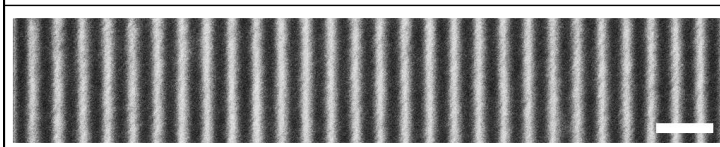	428.4	15
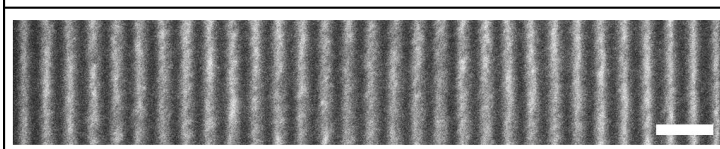	399.8	14
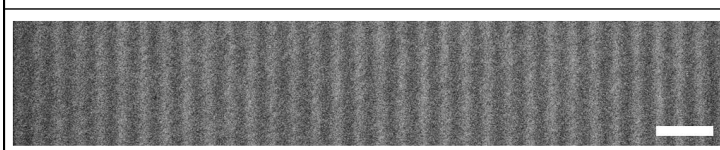	371.3	13

Figure 2-4. Grating patterns generated by proposed digital photolithography system.

2.2. Fabrication process of air-bridge photonic crystal

Because it was identified that the resolving power to manufacture a photonic device was sufficiently secured, the air-bridge photonic crystal device was fabricated using proposed digital photolithography system. The silicon nitride hard mask was deposited on the InGaAsP MQW epilayer, and the photoresist was spin-coated. After the exposure of the photonic crystal pattern using the proposed system, the pattern was transferred to the MQW epilayer through continuous dry etching. Final airbridge device was completed through wet etching. Figure 2-5 shows the overall fabrication process and the SEM image of the device.

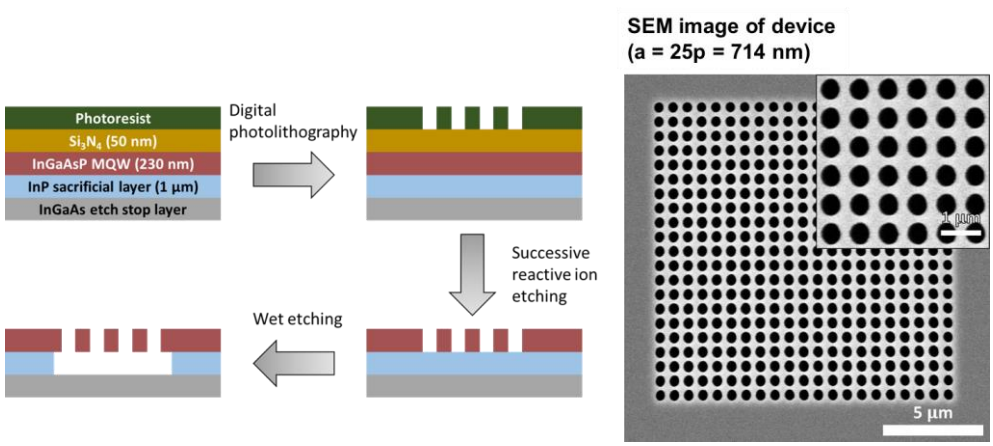

Figure 2-5. Overall fabrication process and SEM image of the fabricated device.

2.3. Square-lattice photonic crystal laser device

Because lattice symmetry of the square-lattice photonic crystal is similar to that of the DMD, it was fabricated first. Figure 2-6 shows the photonic band structure of square-lattice photonic crystal. Numerical simulations, based on the FDTD method, were performed using a commercial software package (FDTD Solutions, Lumerical Solutions). For the band structure calculations, multiple dipole sources were randomly distributed based on their positions, polarization directions, and phases. Bloch boundary conditions were applied along the lateral directions, while the upper and lower boundaries of the simulation field were capped using perfectly matching layers. The spatial resolution was set to 41 pixels per micron. The imaginary parts of the dielectric constants of the composing materials were not considered throughout the simulations, assuming that the optical excitation occurred just above the lasing threshold so that the MQWs became optically transparent without any optical loss or gain.

The normalized frequency of Γ_1 band-edge mode is approximately 0.47 and the lattice constant that causes Γ_1 band-edge mode to overlap with the optical gain band of the MQW is approximately 700 nm. Therefore, two cases in which the hole pattern had a lattice constant of near 700 nm was considered (Figure 2-7). One hole was defined with 12 on-pixels and the distances between the centers of adjacent holes were set to 25 and 24 pixels. The fabricated devices were optically excited using a pulsed, 1064 nm laser diode at 1% duty cycle and exhibited single-mode lasing (Figure 2-8).

Figure 2-9 shows the output intensity of lasers based on the optical pumping intensity for a device with the lattice constant of 25 pixels that exhibits sharp laser turn-on with a clear threshold at approximately 1.2 kW/cm^2, comparable to that of a similar BEL device previously fabricated by our group via EBL [33]. The spectrum near the threshold exhibits three distinct emission peaks, which correspond to the three Γ-point band-edges, whereas Γ_1 mode is dominant above the threshold.

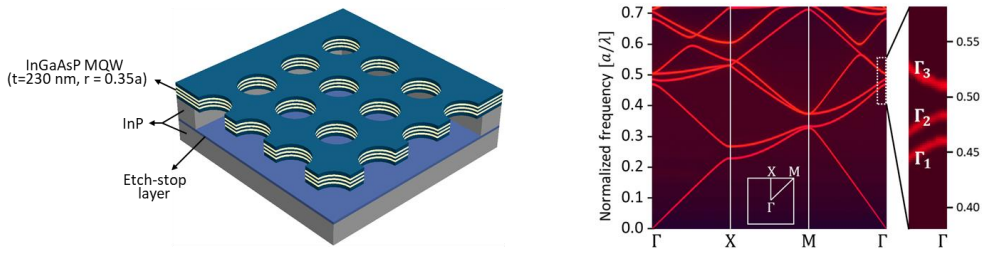

Figure 2-6. Photonic band structure of square-lattice photonic crystal for r = 0.35a.

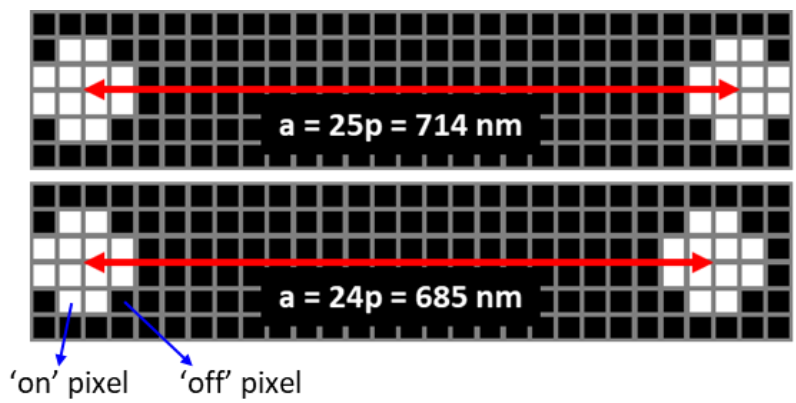

Figure 2-7. Two cases of DMD pixel layouts.

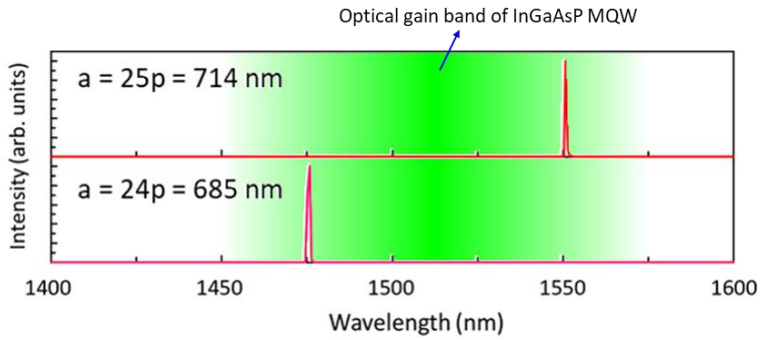

Figure 2-8. Measured photoluminescence of Γ_1 band-edge laser.

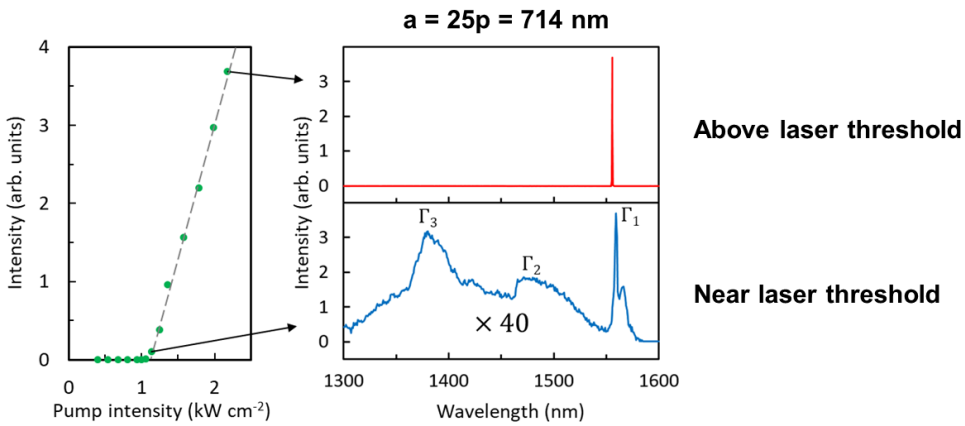

Figure 2-9. Lasing characteristics of square-lattice photonic crystal laser.

Chapter 3

Fine-tuning the lattice constant: patten tilting

3.1. Introduction

3.1.1. Wavelength division multiplexing application

As aforementioned, the two DMD pixel layouts exposed were 25 and 24 pixels of lattice constants. The difference in lattice constant between the two devices is 29 nm, which corresponds to the pixel pitch on the image plane (Figure 3-1). Owing to the difference in the lattice constant, the laser wavelength of the two devices differed by 75 nm which should be reduced to 20 nm or less for applications, such as wavelength division multiplexing [34]. Pattern tilting was proposed as a method to reduce channel spacing.

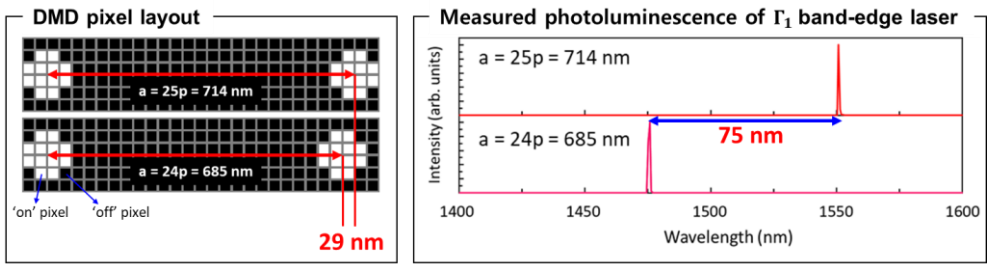

Figure 3-1. DMD pixel layout and measured photoluminescence of laser device.

3.1.2. Pattern tilting

Figure 3-2 shows the pattern tilting. The right hole which was initially apart from the left hole by 24 pixels was vertically shifted by 5 pixels. The resultant hole-to-hole distance is expressed as $(24^2 + 5^2)^{0.5}p \approx 24.52p$, which is greater than 24p but smaller than 25p. By arranging the other hole patterns, a square-lattice PhC structure with a new lattice constant $a \approx 24.52p$ can be generated. That is, the digital nature of DMD can be partially overcome by pattern tilting.

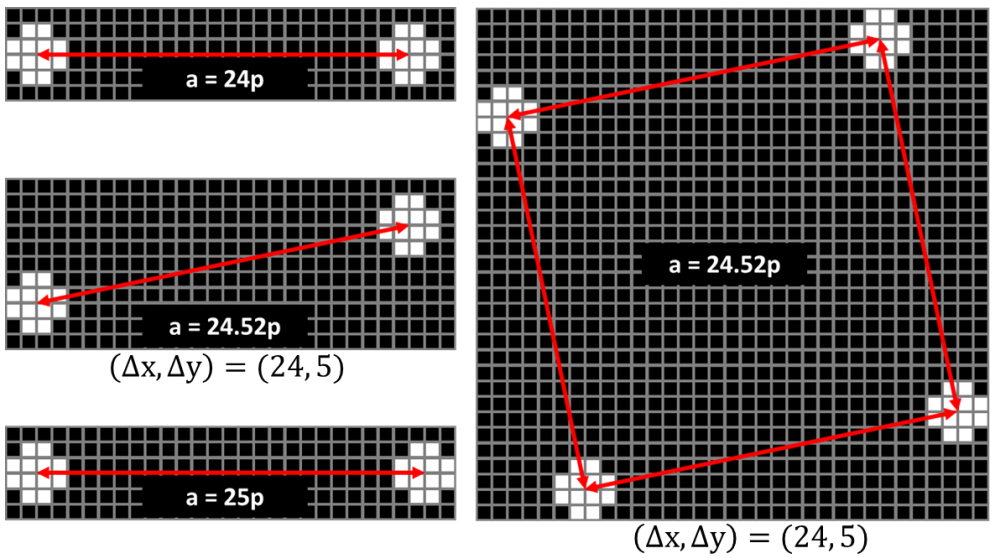

Figure 3-2. Pattern tilting and modulated lattice constant.

3.1.3. All possible tilting configurations

Figure 3-3 shows all possible tilting configurations which can be produced through pattern tilting between 24p and 25p. A total of 15 possible tilting configurations are possible, which reduce lattice constant step from 29 nm to 1.78 nm.

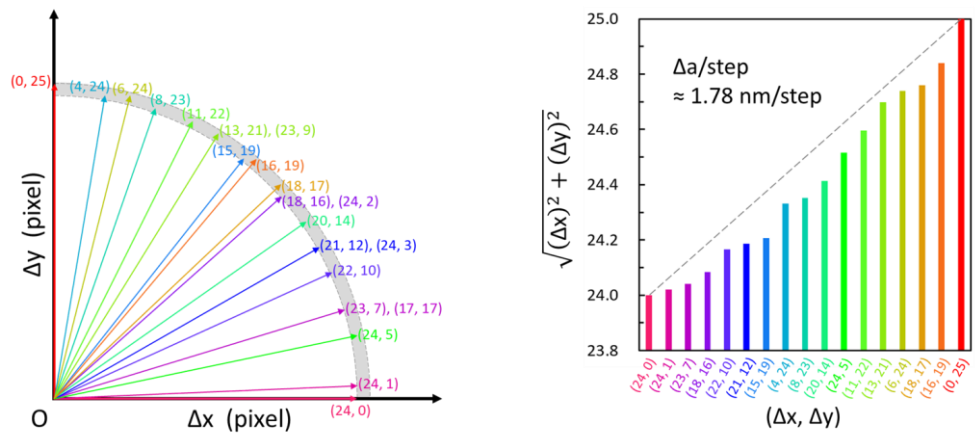

Figure 3-3. All possible tilting configurations between 24p and 25p.

3.2. Result and discussion

3.2.1. Tilting square-lattice

Figure 3-4 shows the square-lattice photonic crystal laser devices which were developed by applying pattern tilting. Five devices were fabricated and arranged in the decreasing order of lattice constant from top to bottom. An enlarged image of each device was inserted as insets on both sides. The top and bottom configurations have the lattice constant that is an integer multiple of the pixel because pattern tilting is not applied and the middle three configurations have the lattice constant that is not an integer multiple of the pixel with pattern tilting. It has been confirmed that as the lattice constant shortens, the lasing wavelength decreases, as predicted by the FDTD simulation. In this manner, when pattern tilting is used, the channel spacing can be reduced to the point where wavelength division multiplexing is possible.

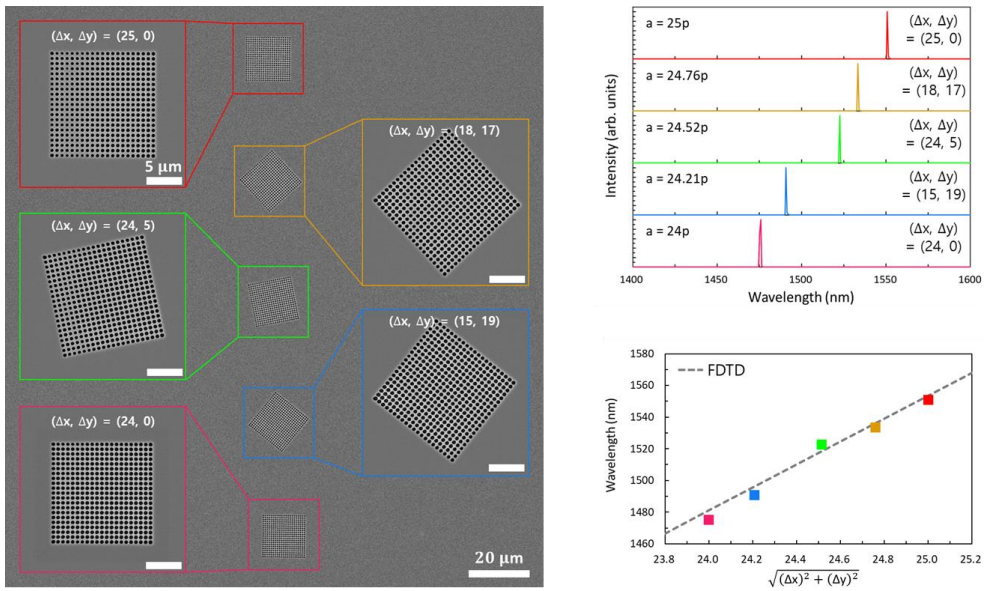

Figure 3-4. Square-lattice photonic crystal laser devices with pattern tilting.

3.2.2. Tilting hexagonal-lattice

Owing to the inconsistency of the lattice symmetry, designing hexagonal lattice is more complicated than square lattice. Figure 3-5 shows the generation of pseudo-hexagonal lattice with some limitations. To arrange the three holes, two holes are set to P1 and P2 with 30 pixels spacing where the red triangle is the equilateral triangle with a side length of 30 pixels. The location of the remaining hole should be P3, which is the yellow dot represented on the inset. However, because of the digital nature of the DMD, the hole center cannot be placed at the position which is not a grid point. On the contrary, P3A that is closer to the yellow dot may be selected among adjacent grid points P3A and P3B. Figure 3-5 shows the SEM image after selecting P3A. The smaller the distance between P3 and P3A, the closer the pseudo-hexagonal lattice is to the ideal hexagonal-lattice.

Similar to the case of the square-lattice, pattern tilting can be applied when designing hexagonal lattice. Figure 3-6 shows the case when the distance between P1 and P2 is not an integer multiple of the pixel. P3D nearest to P3 was selected as an alternative to create the pseudo-hexagonal lattice.

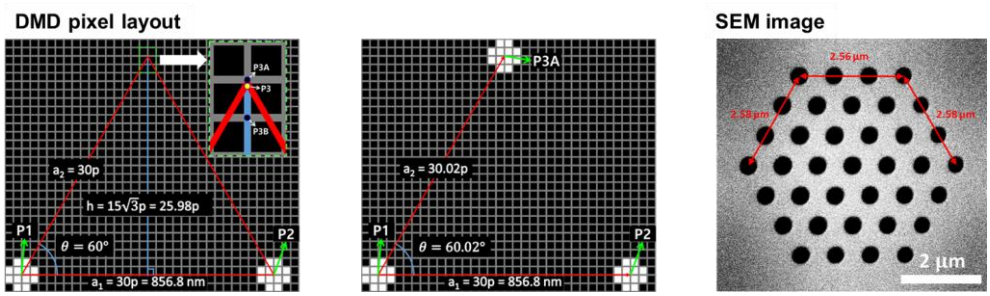

Figure 3-5. DMD pixel layout for pseudo-hexagonal lattice and corresponding SEM image of fabricated photoresist pattern.

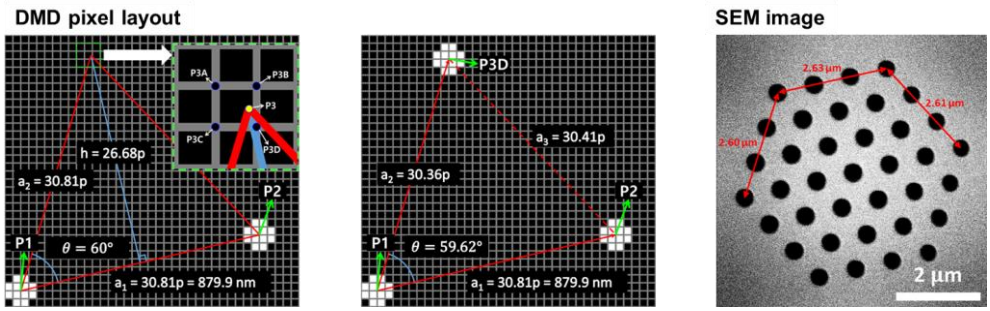

Figure 3-6. The case of pseudo-hexagonal lattice with pattern tilting.

Chapter 4

Fine structural tuning: grayscale exposure

4.1. Introduction

4.1.1. Implementation of gray pixel

The brightness of each pixel can be adjusted individually when performing digital photolithography. Gray pixels can be implemented by dividing the time between pixel on-state and pixel off-state. Creating inclines [19] or printing grayscale images on proteins using photobleacing have been reported [16].

The grayscale exposure was used to arbitrarily adjust the position of the hole. Figure 4-1 shows how to apply grayscale exposure for this purpose. On the pixel space, a virtual hole composed of 12 virtual pixels is marked with a red dotted line. The brightness is assigned to each pixel, proportional to the area where each pixel overlaps the virtual hole. By repeating this for all pixels, the brightness assignment can be completed.

Whether the grayscale exposure is applied or not, the sum of the brightness values of the pixels of one hole is equal to $255 \times 12 = 3060$, indicating that this method only adjusts the position of the hole without changing the hole size.

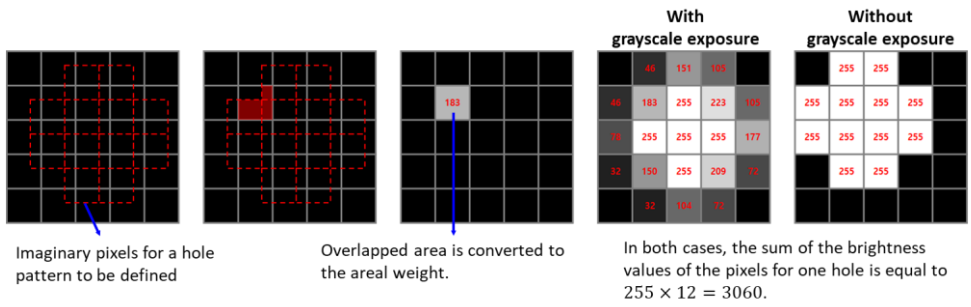

Figure 4-1. Map for grayscale exposure.

4.2. Result and discussion

4.2.1. Grayscale exposed square-lattice

First, the lattice constant of the square-lattice photonic crystal device was finely adjusted using grayscale exposure. Five layouts are shown in decreasing order of lattice constant, including two layouts (top and bottom) with no grayscale exposure (Figure 4-2). The insets are enlarged images of the holes in the lower right corner. Based on the grayscale exposure, the position of the center of the hole marked with a red circle gradually moves.

All of the band-edge laser devices exhibit single-mode lasing with optical pumping, and their spectral positions gradually shift to shorter wavelengths as the PhC lattice constant decreases (Figure 4-3).

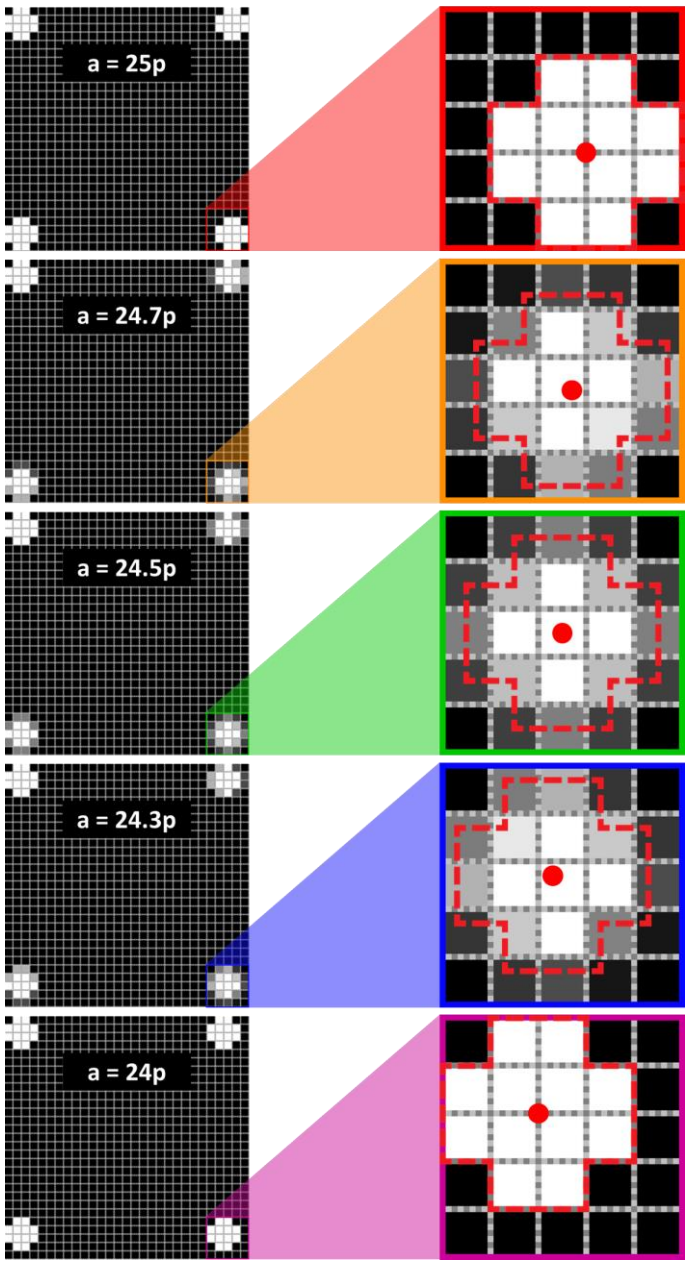

Figure 4-2. Five DMD pixel layouts with finely controlled pattern periods through grayscale exposure.

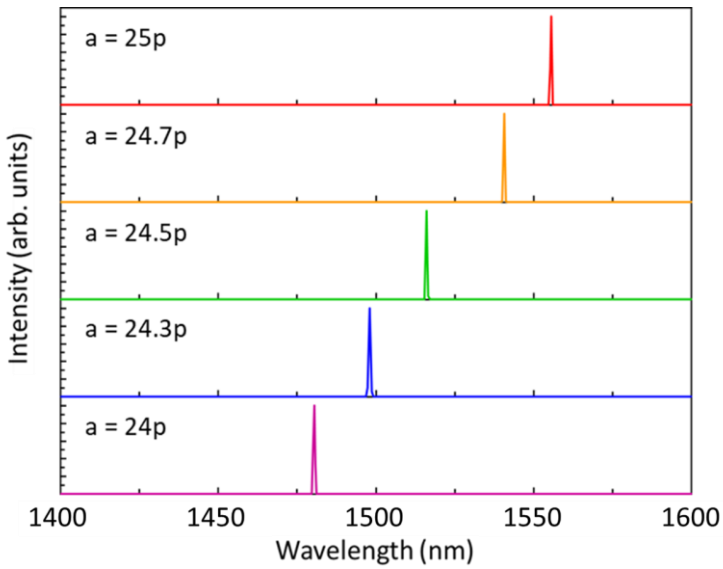

Figure 4-3. Measured photoluminescence of five laser devices.

4.2.2. Grayscale exposed hexagonal-lattice

Not only can the lattice constant be finely adjusted using the grayscale exposure, but it is also possible to generate arbitrary lattices, including the hexagonal lattice. Based on the band structure calculation, the lattice constant is set to 16.7 pixels so that the K_1 band edge mode can overlap with the optical gain band. Figure 4-4 shows the SEM image of the fabricated device and its lasing oscillation. As a result of the optical pumping, single mode lasing was observed and the polarization distribution measured for the BEL emission indicates band-edge lasing action at the K-point. In this manner, when combined with pattern tilting and grayscale exposure, the proposed digital photolithography system transforms into a versatile technique capable of producing submicron-scale photonic device.

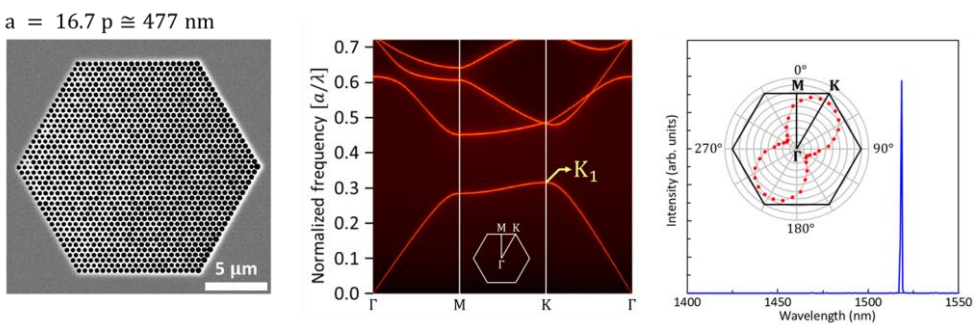

Figure 4-4. Lasing of hexagonal-lattice photonic crystal device.

Chapter 5

Enhancing pattern uniformity

5.1. Introduction

5.1.1. Airy disk point spread function

When the light from the point light source of the object plane is imaged on the image plane, it passes through a series of imaging optical systems and forms the Airy disk point spread function (Figure 5-1). To quantitatively analyze spatial exposure intensity profile on the image plane, each DMD pixel was approximated by point-like light source and corresponding point spread function was introduced (Figure 5-2).

In the case of the ideal point light source with a size of zero, the exposure intensity profile along the line segment passing through the center of the light source shows the point spread function on the image plane (Figure 5-3). However, the actual DMD pixel size is not zero. It is assumed that one DMD pixel on the object plane passes through the imaging optical system to form the Airy disk whose width is widened by B, referred to as broadening factor. Numerical modeling was conducted by setting the widened Airy pattern as the pixel spread function corresponding to the spread function for single pixel.

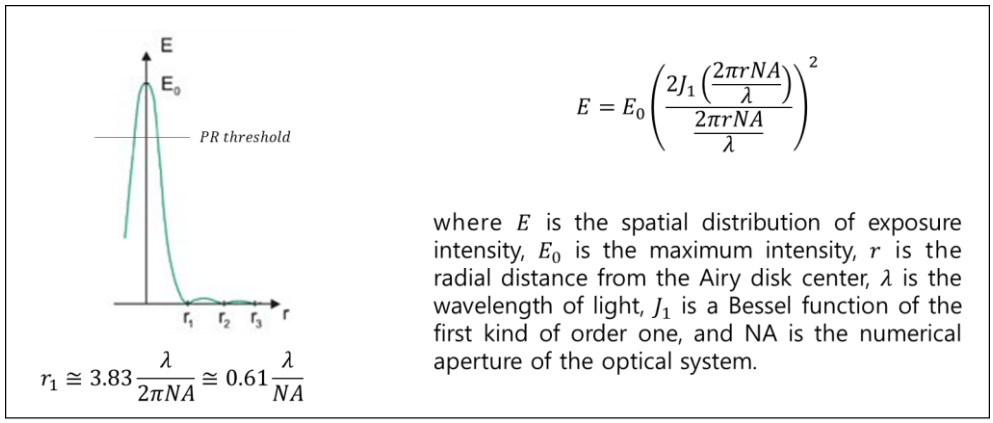

Figure 5-1. Airy disk point spread function [35].

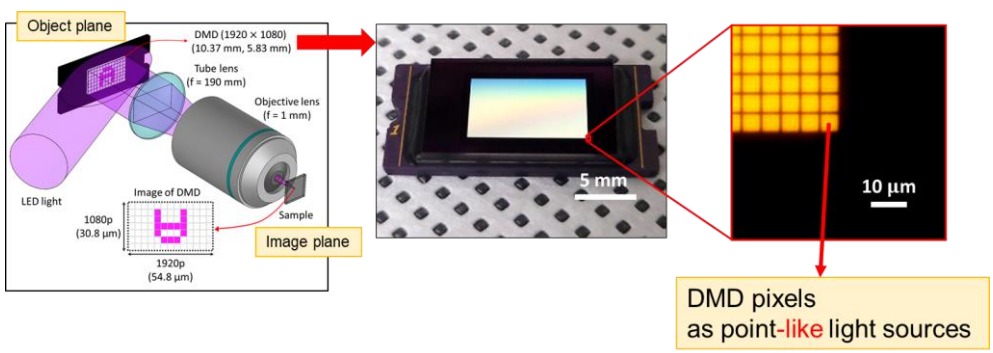

Figure 5-2. Each DMD pixel was approximated by point-like light source.

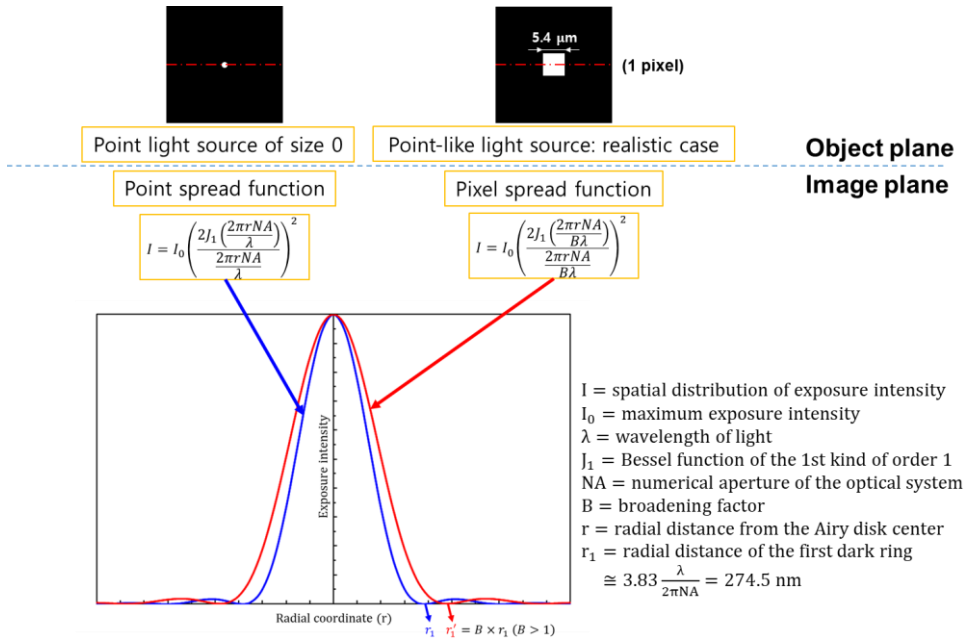

Figure 5-3. Point spread function of ideal case and pixel spread function of realistic case.

In the Figure 5-4, one hole is composed of 21 on-pixels. In the image plane, the exposure dose profile of one hole can be obtained as a linear superposition of the individual pixel spread functions [24]. Because each peak of exposure dose of one pixel is separated by one pixel in the horizontal direction, each peak overlaps with an interval of 28.56 nm which is the pixel pitch of the image plane. Therefore, the peak of the exposure dose of one hole island is smaller than 21 times the peak of the exposure dose of one pixel.

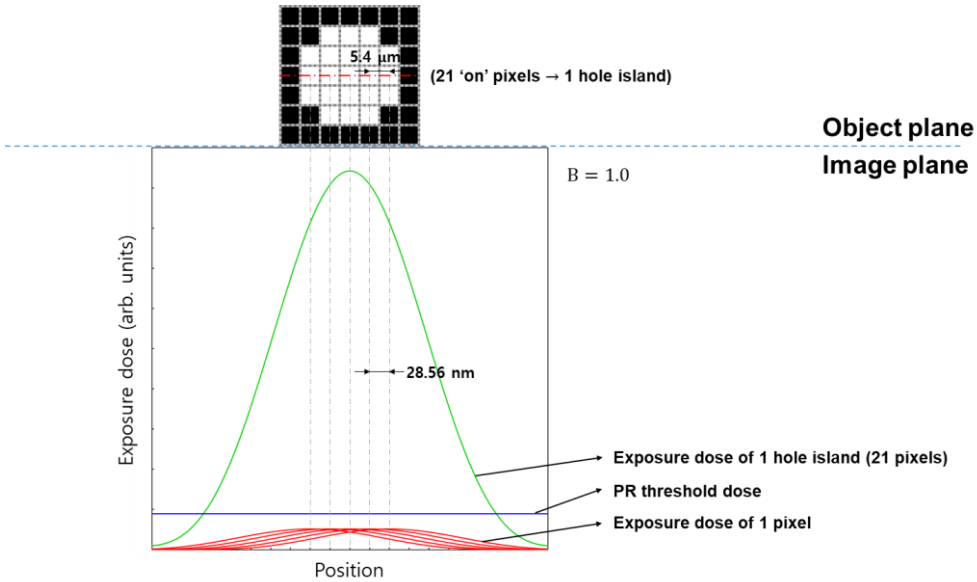

Figure 5-4. Superposition of pixel spread functions.

5.1.2. Broadening factor and exposure dose profile

The broadening factor can be determined experimentally. For example, based on the hole size measured at specific exposure time (t_a), the positional relationship between the exposure dose profile and the photoresist threshold can be set, as shown in Figure 5-5. When the exposure time is reduced by half, the larger the broadening factor, the smaller the predicted hole size. That is, the broadening factor can be determined by changing the hole size over exposure time.

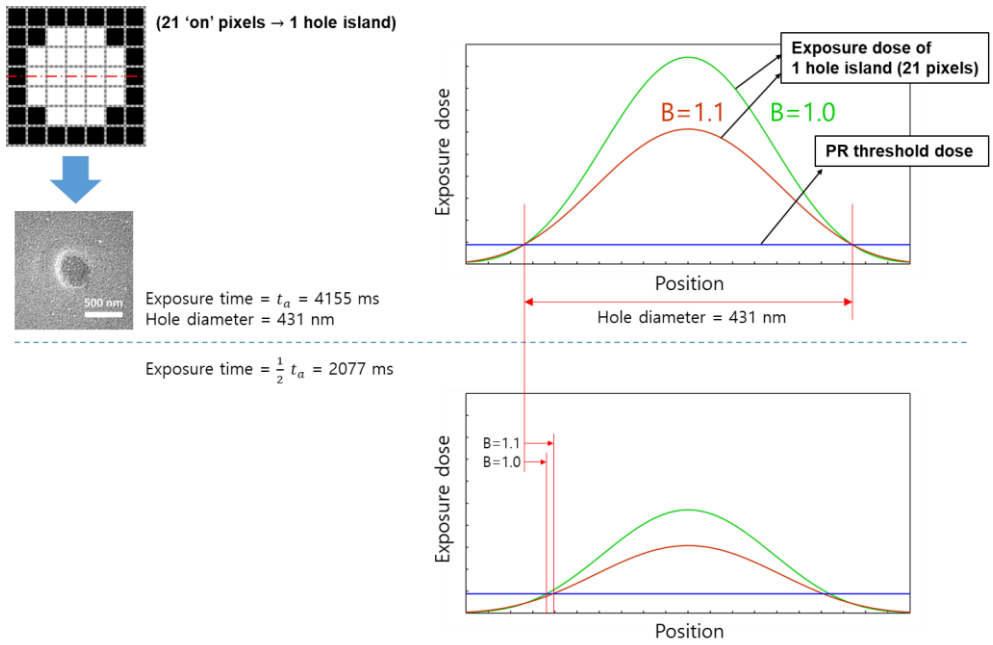

Figure 5-5. The concept that the broadening factor can be determined experimentally.

5.1.3. Experimental determination of broadening factor

Because the exposure time was increased, the size of the fabricated air holes on the photoresist coated on silicon substrate was measured and marked with red dots on the graph shown in Figure 5-6. As a result of performing the simulation by changing the broadening factor, it was confirmed that the simulation and the SEM measurement matched well when the broadening factor was 1.4.

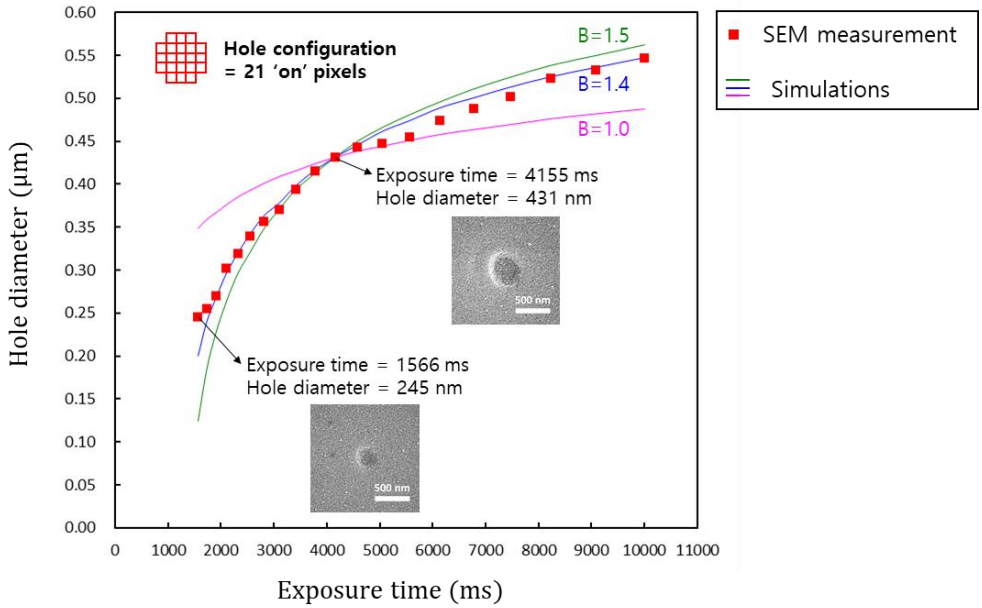

Figure 5-6. Changes in developed hole size over exposure time.

5.2. Result and discussion

5.2.1. Diffraction simulation based on pixel spread function

After determining the pixel spread function, diffraction calculations for the DMD pixel layout were performed (Figure 5-7). The exposure result for the hexagonal photonic crystal-based L3 cavity, can be predicted by considering the portion above the PR threshold.

Figure 5-8 shows the SEM image measured after the exposure and the simulation results. In addition, the overlapped image is displayed between the two images. When the hole pattern is exposed using the digital photolithography system, the hole size varies based on the number of neighboring holes. The holes in Figure 5-8 can be classified into four groups based on the number of neighboring holes. According to the simulation, the larger the number of neighboring holes, the larger the hole size.

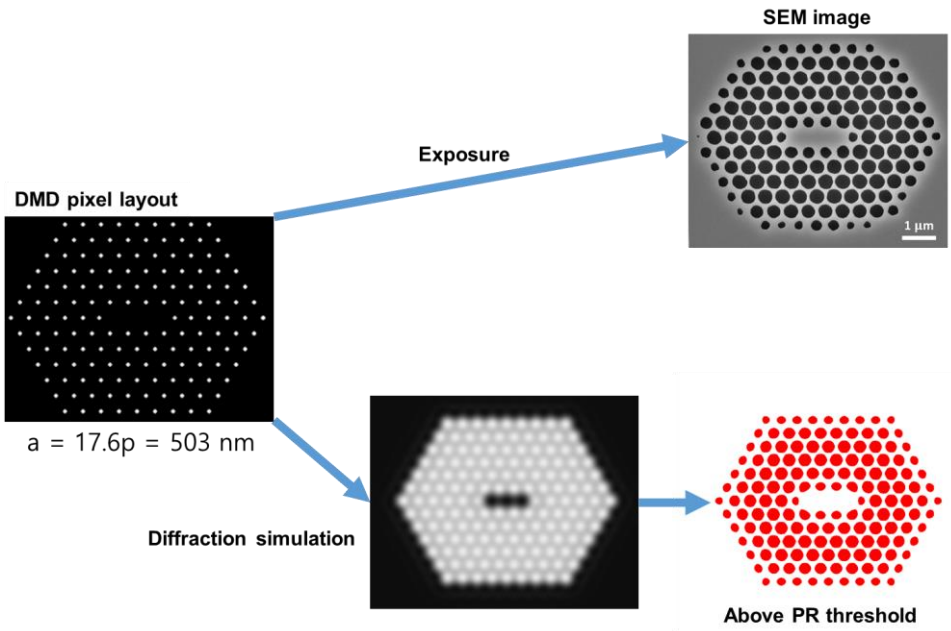

Figure 5-7. Using diffraction simulation, the exposure result can be predicted.

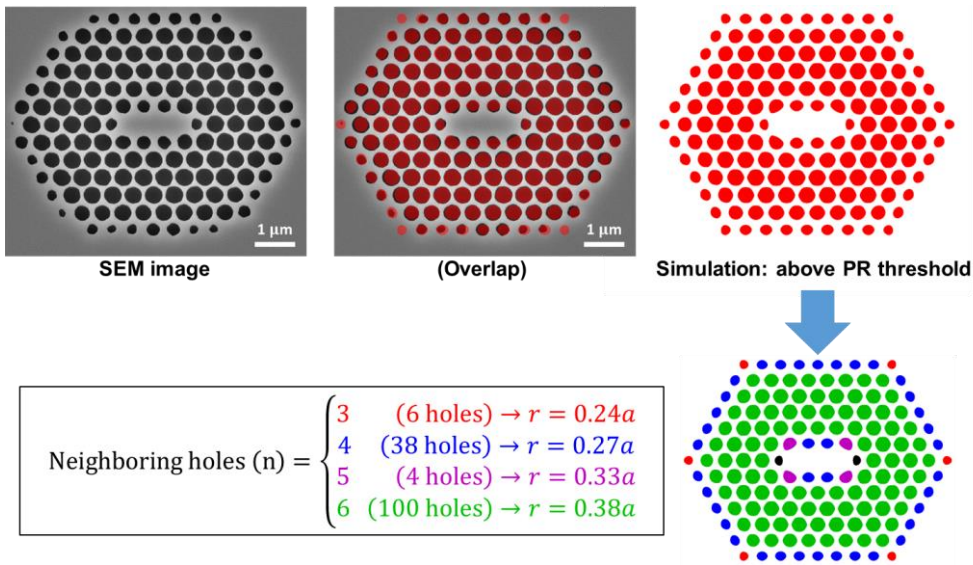

Figure 5-8. Hole size varies based on the number of neighboring holes.

When compared to the fabricated sample, the simulation and fabricated sample exhibit a similar trend (Figure 5-9). In the case of L3 cavity, all holes except two on both sides are designed to be the same size. When the holes above and below the cavity or the outer holes become smaller, Q factor of the cavity mode decreases, which is detrimental to lasing. Therefore, the correction should be performed to make the hole size uniform.

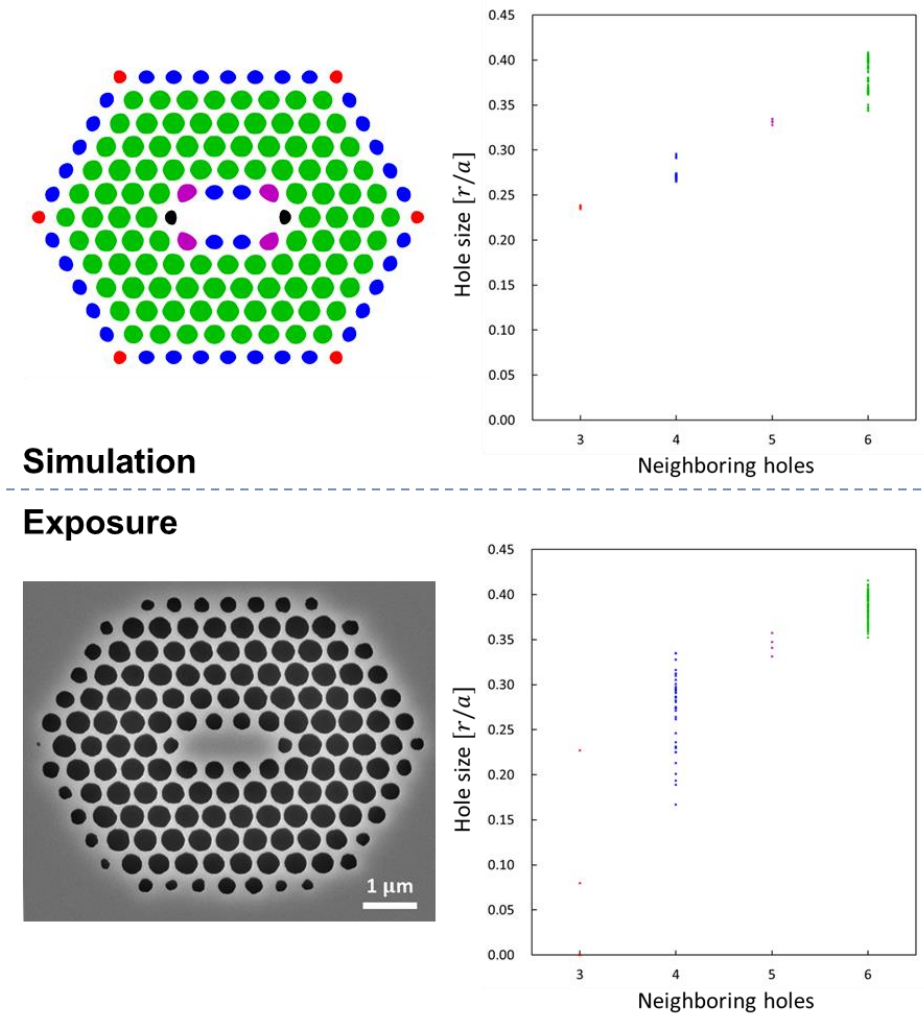

Figure 5-9. Hole size statistics for simulation and fabricated samples.

5.2.2. Correction strategy

To correct the hole size, we calculated how the hole size changes as the brightness is adjusted. Figure 5-10 shows the change in hole size over brightness adjustment. To equalize the different hole sizes, the strategy of reducing the brightness for holes with n = 5, 6 and increasing the brightness for holes with n = 3, 4 was devised. Specifically, to adjust r/a of all holes to 0.3, the brightness should be adjusted by +7.59%, +2.74%, -2.56%, and -5.09% for holes with n = 3, 4, 5, and 6, respectively.

For the DMD pixel layout to which the proposed correction was applied, the diffraction simulation was performed again. According to the simulation result, if proposed strategy is applied, the uniformity will improve.

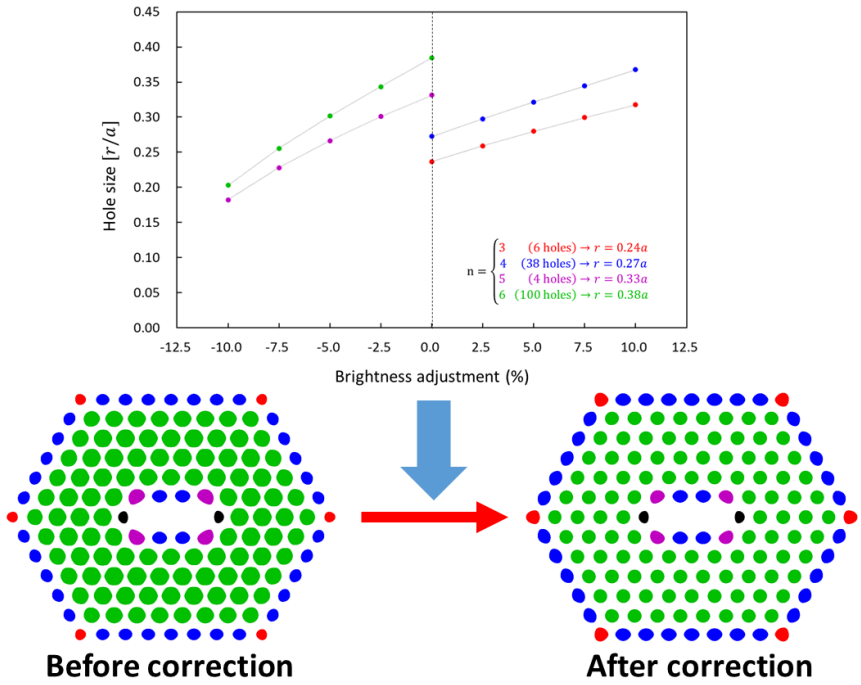

Figure 5-10. With appropriate brightness adjustment for each group, the uniformity is expected to improve.

5.2.3. Analysis of correction result

Figure 5-11 shows the photoluminescence of the three devices. In the case of digital photolithography without correction, laser oscillation fails owning to the decrease in Q factor with the reduction in the size of the holes along the outline of pattern and near the cavity. In the case of digital photolithography with correction, single-mode lasing was measured. The device with the same design was fabricated by e-beam lithography. Comparing the hole size statistics, better lasing characteristic was expected because the hole size was more uniform than the device fabricated through corrected digital photolithography.

The lasing threshold of the device fabricated by digital photolithography with correction was 0.84 kW/cm^2 which is approximately 23.5% higher than that of e-beam lithography (Figure 5-12).

However, the hole size uniformity was improved through correction, which influenced whether the laser oscillation was possible. Moreover, comparing the threshold, the pattern quality can be improved to the level comparable to that of e-beam lithography. When producing small devices, precise correction is essential and pixel spread function-based approach is effective.

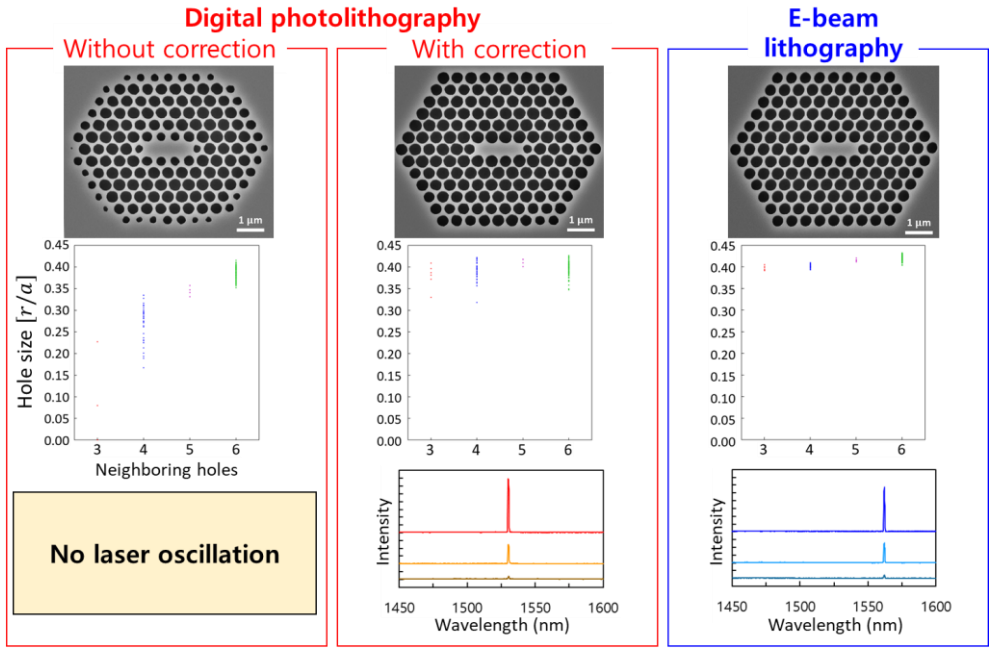

Figure 5-11. The photoluminescence of the three devices.

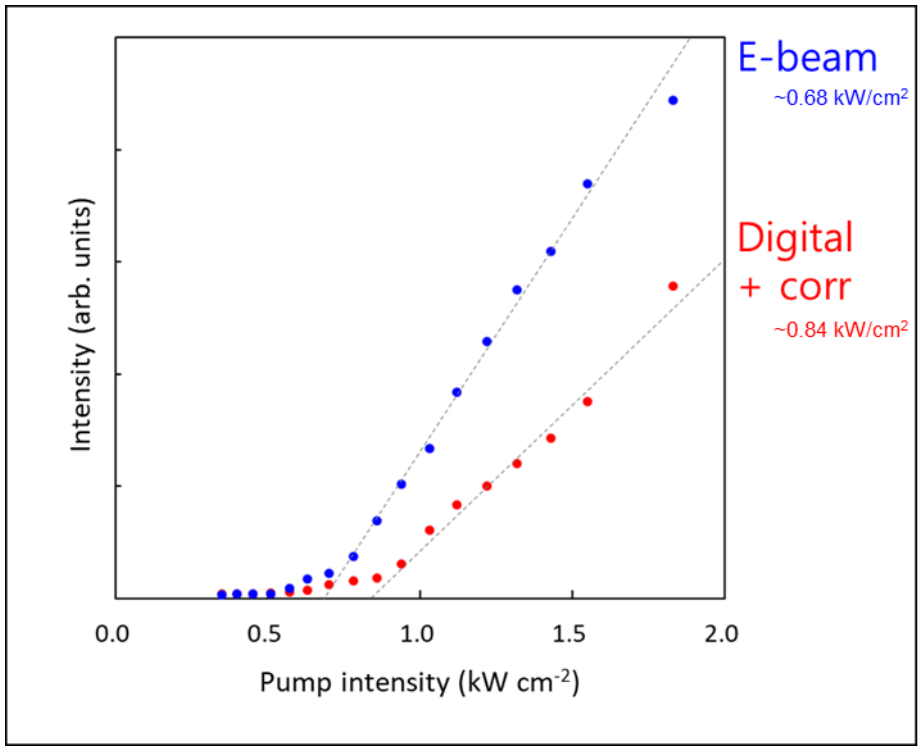

Figure 5-12. Comparison of L-L curves of samples fabricated by e-beam lithography and digital photolithography with appropriate correction.

Chapter 6

Conclusion and perspective

In this thesis, high magnification digital photolithography system was proposed. Several techniques proposed in the thesis were used to specialize this system for submicron pattern fabrication.

First, the pattern tilting that can overcome the digital characteristics of DMD was proposed. Several photonic crystal laser devices were fabricated with finely controlled lattice constant, which made wavelength division multiplexing possible. The lasing wavelength changed as predicted by the FDTD simulation.

Second, the grayscale exposure was proposed as the more general method of controlling the period. The grayscale exposure enabled not only fine control of lattice constant but also generation of arbitrary patterns, including those that are incompatible with the DMD pixel layout, such as hexagonal lattice.

Third, the pixel spread function based on the Airy disk point spread function was introduced to improve exposure pattern quality through numerical analysis of diffraction and appropriate correction. The parameters of the pixel spread function were determined experimentally, and the lasing characteristic of the fabricated device was improved through correction based on the pixel spread function.

Our results shed bright light on the development of low-cost, high-throughput photolithographic equipment, suitable for the low-volume manufacturing of

sophisticated photonic devices that have stringent pattern requirements.

References

[1] E. Yablonivitch, “Inhibited Spontaneous Emission in Solid-State Physics and Electronics,” *Phys. Rev. Lett.* **58**, 2059 (1987).

[2] H. Chang, K. Min, M. Lee, M. Kang, Y. Park, K. Cho, Y. Roh, S. Hwang, and H. Jeon, “Colloidal quantum dot lasers built on a passive two-dimensional photonic crystal backbone,” *Nanoscale* **8**, 6571-6576 (2016).

[3] C. Han, M. Kang, and H. Jeon, “Lasing at multidimensional topological states in a two-dimensional photonic crystal structure,” *ACS Photonics* **7**, 2027-2036 (2020).

[4] M. Kang, C. Han, and H. Jeon, “Submicrometer-scale pattern generation via maskless digital photolithography,” *Optica* **7**, 1788-1795 (2020).

[5] J. D. Joannopoulos, S. G. Johnson, J. N. Winn, R. D. Meade, *Photonic Crystals: Molding the Flow of Light*

(Princeton University Press, 2008).

[6] H. Zheng, and S. Ravaine, "Bottom-Up Assembly and Applications of Photonic Materials," *Crystals* **6**, 54 (2016).

[7] S. Ahn, H. Kim, H. Jeon, J. R. Oh, Y. R. Do, and H. J. Kim, "Two-Dimensional Hexagonal Lattice Photonic Crystal Band-Edge Laser Patterned by Nanosphere Lithography," *Applied Physics Express* **5**, 042102 (2012).

[8] S. Ahn, S. Kim, and H. Jeon, "Single-defect photonic crystal cavity laser fabricated by a combination of laser holography and focused ion beam lithography," *Appl. Phys. Lett.* **96**, 131101 (2010).

[9] M. Altissimo, "E-beam lithography for micro-nanofabrication," *Biomicrofluidics* **4**, 026503 (2010).

[10] H. Kim, H. Jung, D. Lee, K. Lee, and H. Jeon, "Period-chirped gratings fabricated by laser interference lithography with a concave Lloyd's mirror," *Appl. Opt.* **55**, 354-359 (2016).

[11] H. Martinsson, T. Sandstrom, A. Bleeker, and J. D.

Hintersteiner, “Current status of optical maskless lithography,” J. Microlith. Microfab. Microsyst. **4,** 011003 (2005).

[12] Y. Liu, Y. Zhao, X. Dong, M. Zheng, F. Jin, J. Liu, X. Duan, and Z. Zhao, “Multi-scale structure patterning by digital-mask projective lithography with an alterable projective scaling system,” AIP Adv. **8,** 065317 (2018).

[13] R. C. Auyeung, H. Kim, S. Mathews, and A. Pique, “Spatially modulated laser pulses for printing electronics,” Appl. Opt. **54,** F70-F77 (2015).

[14] S. Wen, A. Bhaskar, and H. Zhang, “Scanning digital lithography providing high speed large area patterning with diffraction limited sub-micron resolution,” J. Micromech. Microeng. **28,** 075011 (2018).

[15] J. Kim and K. Jeong, “Batch fabrication of functional optical elements on a fiber facet using DMD based maskless lithography,” Opt. Express **25,** 16854-16859 (2017).

[16] A. Waldbaur, B. Waterkotte, K. Schmitz, and B. E. Rapp, “Maskless projection lithography for the fast and flexible generation of grayscale protein patterns,” Small 8, 1570–1578 (2012).

[17] K. Totsu, K. Fujishiro, S. Tanaka, and M. Esashi, “Fabrication of three-dimensional microstructure using maskless gray-scale lithography,” Sens. Actuat. A 130, 387–392 (2006).

[18] B. Yang, J. Zhou, Q. Chen, L. Lei, and K. Wen, “Fabrication of hexagonal compound eye microlens array using DMD-based lithography with dose modulation,” Opt. Express 26, 28927–28937 (2018).

[19] X. Ma, Y. Kato, F. van Kempen, Y. Hirai, T. Tsuchiya, F. van Keulen, and O. Tabata, “Experimental study of numerical optimization for 3-D microstructuring using DMD-based grayscale lithography,” J. Microelectromech. Syst. 24, 1856–1867 (2015).

[20] Z. Zhang, Y. Gao, N. Luo, and K. Zhong, “Fast

fabrication of curved microlens array using DMD-based lithography," AIP Adv. **6,** 015319 (2016).

[21] Q. Deng, Y. Yang, H. Gao, Y. Zhou, Y. He, and S. Hu, "Fabrication of micro-optics elements with arbitrary surface profiles based on one-step maskless grayscale lithography," Micromachines **8,** 314 (2017).

[22] S. Huang, M. Li, L. Shen, J. Qiu, and Y. Zhou, "Fabrication of high quality aspheric microlens array by dose-modulated lithography and surface thermal reflow," Opt. Laser Technol. **100,** 298–303 (2018).

[23] R. He, S. Wang, G. Andrews, W. Shi, and Y. Liu, "Generation of customizable micro-wavy pattern through grayscale direct image lithography," Sci. Rep. **6,** 21621 (2016).

[24] C. Sun, N. Fang, D. M. Wu, and X. Zhang, "Projection micro-stereolithography using digital micro-mirror dynamic mask," Sens. Actuat. A **121,** 113–120 (2005).

[25] S. Song, K. Kim, S. Choi, S. Han, H. Lee, S. Kwon, and

W. Park, “Fine-tuned grayscale optofluidic maskless lithography for three-dimensional freeform shape microstructure fabrication,” Opt. Lett. **39,** 5162–5165 (2014).

[26] J. Kim, S. Chung, S. Choi, H. Lee, J. Kim, and S. Kwon, “Programming magnetic anisotropy in polymeric microactuators,” Nature Mater. **10**, 747–752 (2011).

[27] S. Habasaki, W. Lee, S. Yoshida, and S. Takeuchi, “Vertical flow lithography for fabrication of 3D anisotropic particles,” Small **11,** 6391–6396 (2015).

[28] R. He, D. Yunus, C. Uhl, W. Shi, S. Sohrabi, and Y. Liu, “Fabrication of circular microfluidic channels through grayscale dual-projection lithography,” Microfluid. Nanofluid. **21,** 13 (2017).

[29] J. Na, N. P. Bende, J. Bae, C. D. Santangelo, and R. C. Hayward, “Grayscale gel lithography for programmed buckling of non-Euclidean hydrogel plates,” Soft Matter **12,** 4985–4990 (2016).

[30] https://heidelberg-instruments.com/

[31] http://www.ti.com/

[32] B. J. Lin, "The k3 coefficient in nonparaxial λ/NA scaling equations for resolution, depth of focus, and immersion lithography," J. Micro/Nanolith. MEMS, MOEMS. **1,** 7–12 (2002).

[33] S. Kim, J. Lee, and H. Jeon, "Over 1 hour continuous-wave operation of photonic crystal lasers," *Opt. Express* **19,** 1–6 (2011).

[34] Edited by H.-J. Thiele and M. Nebeling, *Coarse Wavelength Division Multiplexing: Technologies and Applications* (CRC Press, 2007).

[35] J. E. Greivenkamp, *Field Guide to Geometrical Optics* (SPIE Press, 2008).

Abstract in Korean

디지털 미세거울 장치에 기반한 디지털 포토리소그래피는 차세대 저비용 리소그래피 기술로 여겨진다. 그러나 디지털 미세거울 장치 기반 디지털 포토리소그래피는 주기가 1 마이크론 이상인 패턴 제작시에만 사용되었다. 광자결정레이저 등의 광소자 제작을 위해서는 패턴의 주기가 수백나노미터 수준이어야 하는데, 아직 디지털 포토리소그래피로 이러한 광소자를 제작한 사례는 없었다.

회절 한계를 계산해 보았을 때, 1 마이크론 이하 주기의 패턴 제작이 충분히 가능할 것으로 판단되어, 고배율 결상광학계를 활용하여 디지털 포토리소그래피 시스템을 구축하였다. 구축된 시스템을 사용하여 감광액이 코팅된 시편에 노광을 진행하였으며, 1 마이크론 이하 주기의 패턴 제작이 가능함을 보였다. 마이크로미터 이하 주기의 패턴을 제작할 때, 디지털 포토리소그래피의 패턴 설계 자유도를 향상시키기 위한 두 가지 방법인 패턴 기울임, 회색조 노광을 제안하였으며 실험적으로 시연하였다. 디지털 리소그래피 시스템의 검증에는 광자결정 띠 가장자리 레이저가 주로 사용되었는데, 레이저 발진 여부를 통해 노광 패턴의 품질을 파악할 수 있고 레이저 파장을 통해 노광 패턴의 주기를 파악할 수 있기 때문이다.

또한 픽셀 분산 함수를 도입하여 이미지의 회절 계산 및 패턴 품질 향상을 위한 밝기 보정을 제안하였다. 보정에 의해 패턴의 품질이 크게 향상되어, 전자빔 리소그래피로 제작한 것과 비교할 수 있는 수준이 되었다.

주요어 : 디지털 포토리소그래피, 디지털 미세거울 장치, 광자결정레이저, 광자결정 띠 가장자리 모드

학번 : 2013-20349